J Mater Sci

Ceramics

Crystal structure and microwave dielectric properties of a novel rock-salt type Li_3MgNbO_5 ceramic

Jie Li[1,*], Zhiwei Zhang[1,2], Yunfei Tian[1], Laiyuan Ao[3], Junqi Chen[1], Aihong Yang[1], Congxue Su[1], Laijun Liu[1], Ying Tang[1,2,*], and Liang Fang[1,2,3,*]

[1] *Guangxi Key Laboratory of Optical and Electronic Materials and Devices, College of Material Science and Engineering, Guilin University of Technology, Guilin 541004, China*

[2] *Key Laboratory of Nonferrous Materials and New Processing Technology, Ministry of Education, Guilin University of Technology, Guilin 541004, People's Republic of China*

[3] *College of Materials and Chemical Engineering, China Three Gorges University, Yichang 443002, China*

Received: 13 May 2020
Accepted: 19 August 2020

ABSTRACT

A new rock-salt type compound, namely Li_3MgNbO_5, was synthesized using traditional two-step sintering process for the first time. The products were characterized by X-ray diffraction (XRD), transmission electron microscopy (TEM), scanning electron microscopy (SEM), and thermal dilatometer and network analyzer. The Li_3MgNbO_5 ceramic sintered at 1260 °C adopted a cubic structure with Fm-3 m space group and exhibited excellent microwave dielectric properties (MDPs) of $\varepsilon_r = 16.2$, $Q \times f = 96796$ GHz, and TCF = − 24.8 ppm/°C. The fitting results of the infrared spectrum indicated that the dielectric polarization of Li_3MgNbO_5 in microwave frequency band was contributed by phonon absorption in infrared band. Furthermore, the negative TCF value of Li_3MgNbO_5 ceramic was compensated with a traditional TCF compensator ~ $CaTiO_3$. A near-zero TCF value of + 1.2 ppm/°C was achieved in the composite $0.96Li_3MgNbO_5$–$0.04CaTiO_3$ ceramics with $\varepsilon_r = 18.4$ and high $Q \times f = 86625$ GHz, exhibiting a great potential to be applied in microelectronics systems.

Introduction

Dielectric ceramics with excellent combination of dielectric properties making them suitable for applications in microwave communication systems as resonators, filters, and antenna substrates have been extensively studied in the last half century [1–3]. For applications, dielectric ceramics require a low dielectric loss or high quality factor ($Q \times f$), a near-zero temperature coefficient of resonant frequency (TCF), and an appropriate relative permittivity (ε_r). With the advancement of wireless communication

Handling Editor: Shen Dillon.

Address correspondence to E-mail: jielee2019@aliyun.com; tangyinggl001@aliyun.com; fanglianggl001@aliyun.com

https://doi.org/10.1007/s10853-020-05141-0

Published online: 27 August 2020

toward high-frequency microwave and millimeter wave range, higher Q microwave ceramics are strongly desired [4, 5]. Some low-loss dielectric ceramics, such as Al_2O_3, Mg_2SiO_4, $Ba(Mg_{1/3}Ta_{2/3})O_3$, and $Ba(Zn_{1/3}Ta_{2/3})O_3$, have been applied in microelectronics systems over the past decades [6–9]. However, the issues of high sintering temperature (> 1300 °C) and expensive raw materials (Ta_2O_5) are not enabling the long-term commercialization of these dielectrics. Therefore, it becomes of greater interest to develop microwave dielectric ceramics which are nontoxic, low cost combined with high Q values.

In recent years, the Li_2O–MgO–TiO_2 ternary system microwave dielectric materials with cubic rock-salt structure have gained considerable attentions owing to their high Q values and low cost [10–18]. Such ternary rock-salt type compounds can be, in fact, considered as solid solutions formed by Li_2TiO_3–MgO. In 1979, A.R. West disclosed a phase transition from monoclinic Li_2TiO_3 phase to cubic MgO phase when x was beyond 0.4 in $(1-x)Li_2TiO_3$–xMgO system [19]. Afterward, a series of MgO-type solid solution [(MgO)ss] materials with Fm-3 m space group were reported, such as Li_2MgTiO_4 ($0.5Li_2TiO_3 + 0.5MgO$), $Li_4Mg_3Ti_2O_9$ ($0.4Li_2TiO_3 + 0.6MgO$), $Li_2Mg_2TiO_5$ ($1/3Li_2TiO_3 + 2/3MgO$), $Li_6Mg_7Ti_3O_{16}$ ($0.3Li_2TiO_3 + 0.7MgO$), $Li_2Mg_3TiO_6$ ($0.25Li_2TiO_3 + 0.75MgO$), $Li_2Mg_4TiO_7$ ($0.2Li_2TiO_3 + 0.8MgO$) [11–16]. Of special note is that at least 49.6% increase in $Q \times f$ values for the (MgO)ss mentioned above than that of pure Li_2TiO_3 ceramic. The reason may lie in the fact that the microcrack and (001) cleavage plane disappeared as (MgO)ss formed, leading to a significant reduction in dielectric loss [20]. The similar results were also found in Li_2SnO_3–MgO and Li_2ZrO_3–MgO systems [21–24].

Li_3NbO_4 belongs to a cubic rock-salt structure with I-43 m space group, which possessed a good MDPs of $\varepsilon_r = 16.4$, $Q \times f = 47179$, $\tau_f = -45$ ppm/°C [25]. Hence, a wide range of solid solutions would be expected in Li_3NbO_4–MgO system due to their same crystal structure and similar ionic radii of Li^+ (0.76 Å), Mg^{2+} (0.72 Å), and Nb^{5+} (0.64 Å). Bian et al. have studied the structural evolution and MDPs of $Li_{3-3x}Mg_{4x}Nb_{1-x}O_4$ system, with a crystal symmetry transition from order cubic (I-43 m) to disorder cubic phase (Fm-3 m) when $0.01 \le x < 1/3$; in the meanwhile, an intermediate compound of $Li_3Mg_2NbO_6$ with orthorhombic structure formed at $x = 1/3$ composition [26]. In the present work, a novel Li_3MgNbO_5 ($0.5Li_3NbO_4 + 0.5MgO$) solid solution ceramic was designed and prepared via solid-state sintering route. Crystal structure and MDPs were evaluated together with its microstructure. Moreover, infrared reflectivity spectroscopy has been conducted to investigate their eigen dielectric properties.

Experimental procedures

Using conventional solid-state sintering process, Li_3MgNbO_5 ceramic was fabricated from high-purity starting materials of Li_2CO_3 (99.99%), MgO (99.99%), and Nb_2O_5 (99.99%). Details of processing procedure are similar with our previous works [27]. Attention should be paid to the fact that the MgO has hygroscopic property and must be calcined at 900 °C for 2 h before weighing. The mixed raw materials were calcined at 1000 °C for 2 h, and the samples were sintered at 1200–1280 °C for 4 h. The phase purity of Li_3MgNbO_5 was examined using an X-ray powder diffraction (Panalytical X'pert Pro diffractometer with Cu Kα radiation). Rietveld refinement was performed using Fullprof software based on the XRD slow scan data. High-resolution transmission electron microscope (HRTEM) images and selected area electron diffraction (SAED) patterns were collected with a JEM-2100F TEM at a working voltage of 200 kV. Microstructures of the polished and thermally etched surfaces of the samples were observed by scanning electron microscope (Model JSM6380-LV SEM, JEOL, Japan), and energy-dispersive spectrometer (EDS) was used to conduct microstructure analysis. The densities of the ceramics were determined using the Archimedes method. The linear coefficient of thermal expansion (α_L) of the ceramics was evaluated by a NETZSCH DIL402C thermal dilatometer. The temperature-dependent dielectric characteristics was measured by an Agilent 4294A precision impedance analyzer equipped with a temperature controller. Room-temperature infrared reflectivity spectrum was recorded using a Bruker IFS 66v FTIR spectrometer on Infrared beamline station (U4) at National Synchrotron Radiation Lab. (NSRL), China. The microwave dielectric properties were measured by an Agilent N5230A network analyzer equipped with a Delta 9039 oven. And the TCF values were calculated using the following formula:

$$\mathrm{TCF} = \frac{\Delta f}{f_0(T_2 - T_1)} \quad (1)$$

here $\Delta f = f_2 - f_1$, f_2 and f_1 were the resonant frequencies at the temperature of T_2 and T_1, respectively.

Results and discussions

XRD patterns of Li_3MgNbO_5 ceramics sintered at different temperatures are illustrated in Fig. 1a. A rock-salt phase with Fm-3 m space group was indexed according to the standard pattern of MgO phase (JCPDS PDF#01-1235), and no evidence of a secondary phase throughout the temperature range. This results indicated that Li and Nb ions diffused into the crystal lattices, forming the solid solutions of which the substitution mechanism could be considered as $Li^+ + Nb^{5+} \rightarrow 3Mg^{2+}$. In addition, the main peak (200) shifted toward lower angle with increasing sintering temperature, indicating the increase in lattice parameters based on the Bragg equation. The evolution of lattice parameters and cell volume of Li_3MgNbO_5 ceramics sintered at different temperatures are listed in Table 1.

Measured and calculated X-ray powder diffraction profiles of the Li_3MgNbO_5 samples sintered at 1260 °C are presented in Fig. 1b: $a = b = c = 4.2138(3)$ Å, $\alpha = \beta = \gamma = 90°$ and $V_m = 74.8207(8)$ Å^3 (R_p = 6.13%, R_{wp} = 8.09%, χ^2 = 2.42). The reliable results of Rietveld refinement supported that Li_3MgNbO_5 adopted a cubic structure with a space group Fm-3 m (No. 225). Table 2 lists the refined atomic fractional coordinates from XRD data. A schematic of the crystal structure of Li_3MgNbO_5 is depicted in Fig. 1d, which can be observed that the Li/Mg/Nb cations occupying 4a Wyckoff position and connecting with the adjacent six O anions. The regular octahedrons coordinated for both cations and anions are edge shared through three-dimensional network. The high-resolution images and SAED patterns (inset)

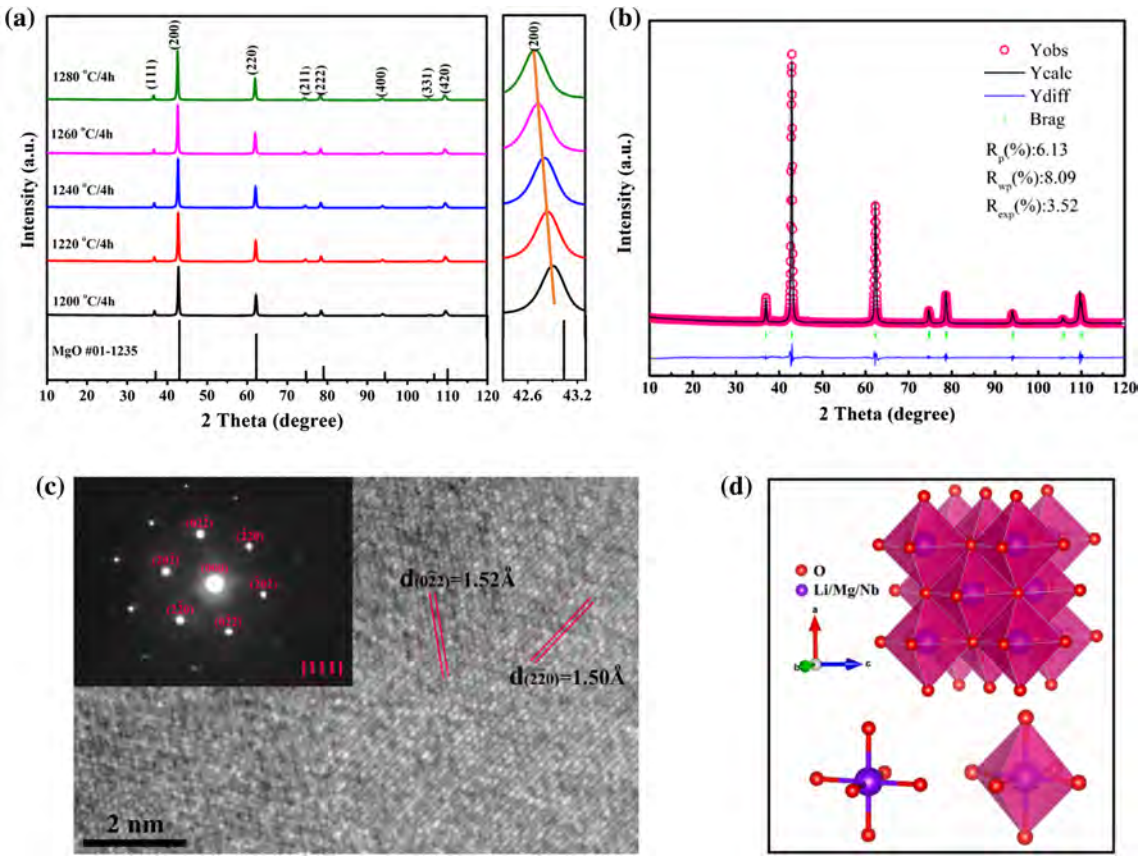

Figure 1 **a** XRD patterns of Li_3MgNbO_5 ceramics sintered at various temperatures; **b** Rietveld refinement of sample sintered at 1260 °C; **c** SAED pattern and HRTEM images of Li_3MgNbO_5 sample sintered at 1260 °C; and **d** schematic of the crystal structure for Li_3MgNbO_5.

Table 1 Lattice parameters, unit cell volume, reliability factors, and goodness-of-fit indicator of Li_3MgNbO_5 ceramics sintered at different temperatures

S.T. (°C)	$a = b = c$ (Å)	V_m (Å^3)	R_p (%)	R_{wp} (%)	χ^2
1200	4.2101 (8)	74.6283 (2)	4.15	6.89	2.25
1220	4.2111 (0)	74.6806 (7)	3.14	8.23	2.12
1240	4.2119 (5)	74.7214 (4)	6.01	7.67	3.13
1260	4.2138 (3)	74.8207 (6)	6.13	8.09	2.42
1280	4.2147 (6)	74.8742 (8)	5.12	7.64	1.98

were recorded along the [111] zone axis to analyze the structure of Li_3MgNbO_5 ceramic (Fig. 1c). The SEAD patterns display regular and bright diffraction spots, which could be ideally indexed based on the face-centered cubic structure with Fm-3 m space group. The characteristic spacings of the (0–22) and (2–20) lattice fringes are 1.52 Å and 1.50 Å, respectively, which is in perfectly agreement with SEAD patterns and XRD data.

Figure 2 demonstrates the SEM images of polished and thermally etched surfaces and the average grain size (AGS) of Li_3MgNbO_5 ceramics as a function of sintering temperature. Many intergranular pores are observed in Fig. 2a and b, which was mainly ascribed to the relatively low sintering temperature, resulting in grain growth insufficient. With the elevation of sintering temperature, the porosity decreased and grain size increased obviously. A relatively few pores and homogeneous microstructure with an AGS of 26.42 μm were obtained in the sample sintered at 1260 °C for 4 h, which was consistent with that of the maximum value of relative density. As the temperature continue to rise, however, abnormal grain growth (AGS:40.14 μm) is observed in Fig. 2e. The reason for this phenomenon may be that the sintering temperature is too high, yielding a large driving force for grain boundary migration, causing some grain boundaries to fuse each other, and forming an abnormal large grain [28, 29].

The changes in bulk density and relative density of the Li_3MgNbO_5 ceramics with sintering temperature are shown in Fig. 3a. The bulk density increased with the increase in temperature, but decreased when the temperature exceeded 1260 °C and then saturated around 3.48 g/cm^3 with a relative density of 95.4%, which was related to the grains growth and the decrease in pores as shown in Fig. 2a–d. The relative density showed a downward trend when temperature increased to 1280 °C, ascribing to the pores in some grain boundaries coated inside larger grains during grain boundary quick migration [28, 29].

Figure 3b shows the variations in ε_r and ε_{corr} of Li_3MgNbO_5 ceramics with temperature ranging from 1200 to 1280 °C. In general, ε_r value is related to relative density and dielectric polarizability and grain boundary [30]. In this study, the ε_r values of Li_3MgNbO_5 ceramics gradually increased with the increase in grain size. The grain size increased, and the grain boundary decreased. Owing to the low dielectric constant of the grain boundary, the dielectric constant of the sample increased with the decrease in grain boundary [31]. And the subsequent slight decline in ε_r might be attributed to the abnormal growth of grains. The variation in ε_r was similar to that of relative density, meaning that the densification level played a dominate role in ε_r. ε_{corr} was calculated using Eq. (2), and the formula is as follows [32]:

$$\varepsilon_{corr} = \varepsilon_{mea}(1 + 1.5P) \quad (2)$$

where P refers to the fractional porosity. Correction of the relative permittivity excludes the effect of pores on it, which is basically stable around 17, higher than the measured value. In addition, the theoretical value of relative permittivity (ε_{th}) can be obtained using the Shannon's additive rule and the Clausius–Mossotti equation [33, 34]:

$$\alpha(Li_3MgNbO_5) = 3\alpha(Li^+) + \alpha(Mg^{2+}) + \alpha(Nb^{5+}) + 5\alpha(O^{2-}) \quad (3)$$

Table 2 Information of atomic space occupying for cubic Li_3MgNbO_5 ceramic

Atom	Wyckoff position	Occupancy	x	y	z	Biso
Li	4a	0.6000	0.0000	0.0000	0.0000	0.38007
Mg	4a	0.2000	0.0000	0.0000	0.0000	0.38007
Nb	4a	0.2000	0.0000	0.0000	0.0000	0.38007
O	4b	1.0000	0.5000	0.5000	0.5000	0.84801

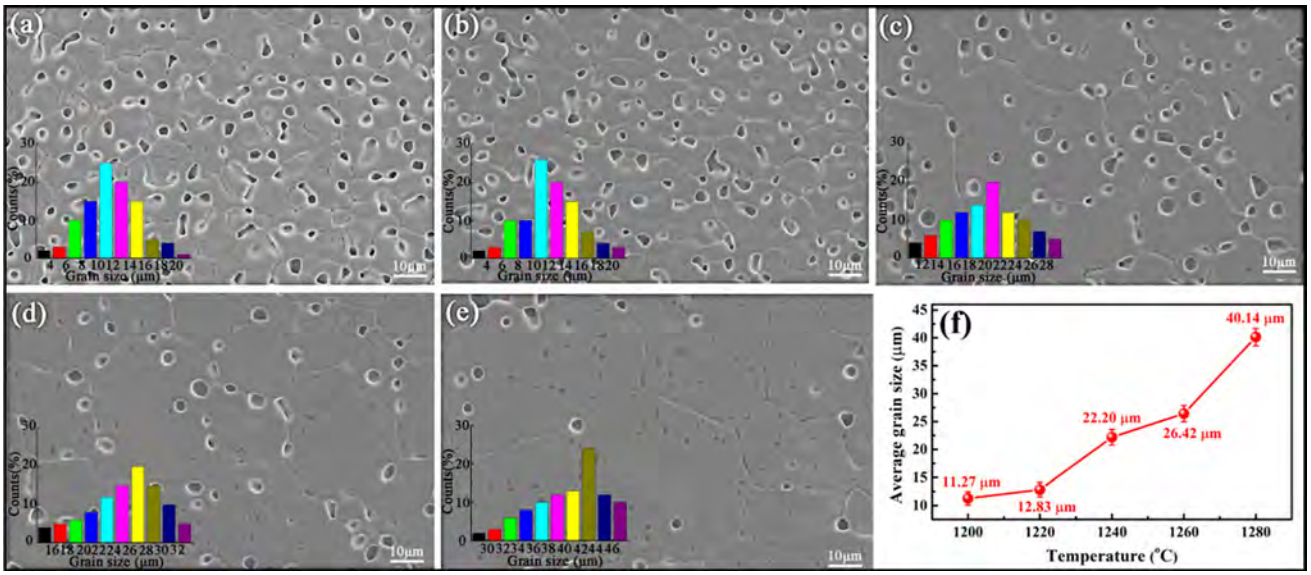

Figure 2 SEM images and the grain size distributions of Li_3MgNbO_5 ceramics sintered at different temperatures for 4 h (**a**–**e** corresponding to 1200–1280 °C); **f** average grain size of Li_3MgNbO_5 ceramics as a function of sintering temperatures.

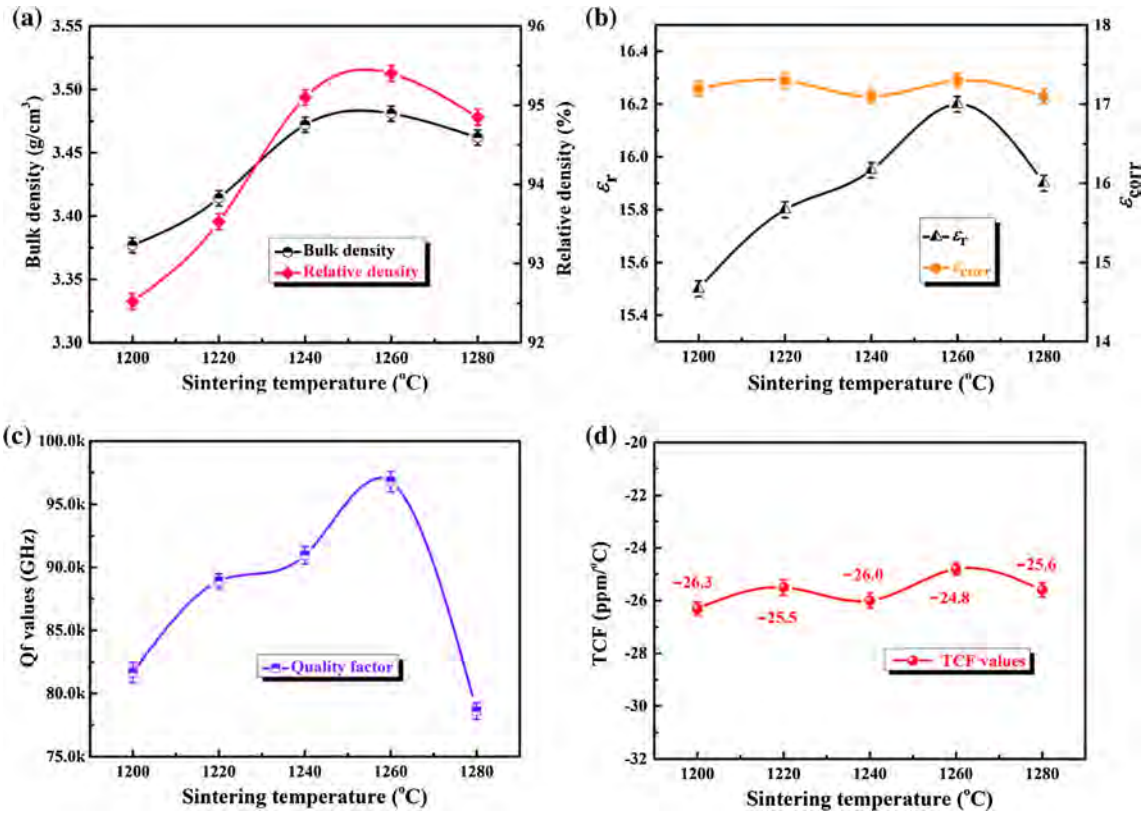

Figure 3 **a** Bulk density and relative density; **b** relative permittivity (ε_r and ε_{corr}); **c** quality factor; and **d** temperature coefficient of resonance frequency (TCF) of Li_3MgNbO_5 ceramics sintered at 1200–1280 °C for 4 h.

$$\varepsilon_{th} = \frac{3V_m + 8\pi\alpha}{3V_m - 4\pi\alpha} \quad (4)$$

where the ionic polarization was set as 1.20 Å^3 for Li^+, 1.32 Å^3 for Mg^{2+}, 3.97 Å^3 for Nb^{5+} and 2.01 Å^3 for O^{2-}, respectively, and V_m represented cell

volume. The theoretical value was equal to 17.77 according to Eqs. (3) and (4), which was comparable to the corrected value. The rise in $Q \times f$ values from 81658 GHz to 96796 GHz was mainly attributed to the improvement in the densification level for Li_3MgNbO_5 ceramics sintered at 1200 ~ 1260 °C. However, a sharp drop in $Q \times f$ value when temperature increased to 1280 °C might be related to the abnormal grain growth, as demonstrated in Fig. 2f, and the AGS surged up from 26.42 to 40.14 μm.

As illustrated in Fig. 3d, the TCF values of Li_3MgNbO_5 ceramics were insensitive to sintering temperature and presented a fluctuation at about − 25 ppm/°C. As is well known, the TCF is closely related to the linear thermal expansion coefficient (α_L) and the temperature coefficient of relative permittivity (τ_ε), which is defined as follows [35]:

$$\mathrm{TCF} = -(\alpha_L + \frac{1}{2}\tau_\varepsilon) \tag{6}$$

Figure 4a presents the thermal expansion curve of Li_3MgNbO_5 ceramic in the range of 25–300 °C. The α_L values is + 4.4 ppm/°C between 25 and 85 °C. Hence, the TCF value is mainly controlled by τ_ε value. Temperature dependence of relative permittivity at four different frequencies is illustrated in Fig. 4b. The inset of Fig. 4b gives the enlarged profile at 25–85 °C measured at 1 MHz, yielding a τ_ε value of + 76.2 ppm/°C. According to Eq. (6), the calculated TCF value was − 42.5 ppm/°C, which was nearly 70% higher than that of measured value at microwave frequency. Besides, it was worth noting that the value of relative permittivity around 18.4 measured at 1 MHz was comparable to the measured value (16.2), which might be due to the dominant role of ion polarization at both frequencies.

It is well known that intrinsic dielectric properties can be predicted, which obtained from the infrared reflectivity spectra extrapolated to the microwave region based on K–K relationship [36]. The infrared reflectivity spectra were analyzed by the classical harmonic oscillator model, the formula as follows [37]:

$$\varepsilon^*(\omega) - \varepsilon_\infty = \sum_{j=1}^{n} \frac{\omega_{pj}^2}{\omega_{oj}^2 - \omega^2 - j\omega\gamma_j} \tag{7}$$

where ε_∞ is the dielectric constant caused by the electronic polarization at high frequencies, γ_j, ω_{oj}, and ω_{pj} are the damping coefficient, the transverse

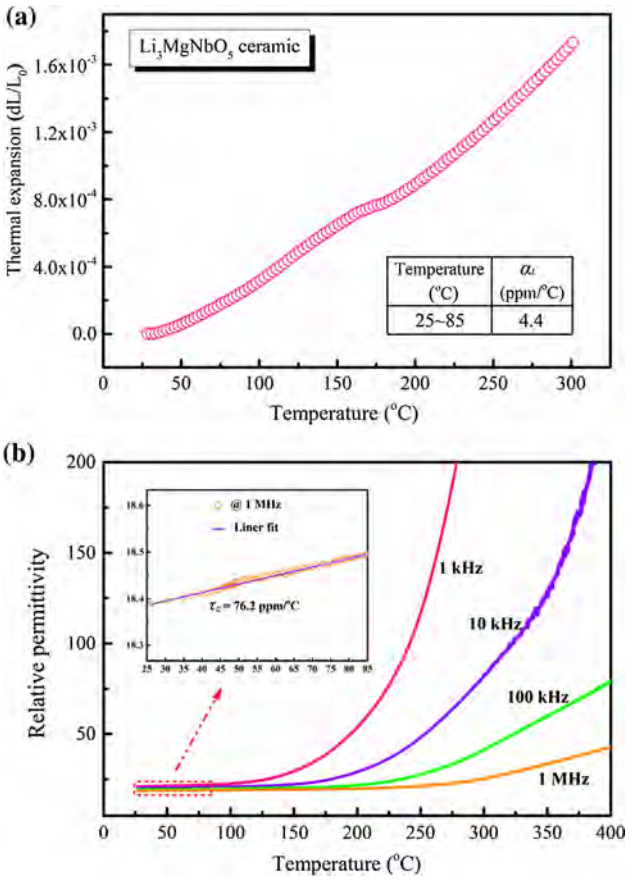

Figure 4 **a** Thermal expansion curve in the temperature range 25 ~ 300 °C of Li_3MgNbO_5 sintered at 1280 °C and **b** dependence of relative permittivity on temperature at four different frequencies (1 kHz, 10 kHz, 100 kHz, and 1 MHz).

frequency and plasma frequency of the *j*th Lorenz oscillator, respectively, and n is the number of transverse phonon modes. The complex reflectivity $R(\omega)$ can be written as:

$$R(\omega) = \left|\frac{1 - \sqrt{\varepsilon^*(\omega)}}{1 + \sqrt{\varepsilon^*(\omega)}}\right|^2 \tag{8}$$

Measured and fitted infrared reflectivity spectra and the real and imaginary parts of complex dielectric response of Li_3MgNbO_5 ceramics are given in Fig. 5, and the relevant phonon parameters are listed in Table 3. As shown in Fig. 5, the measured values of real and imaginary part of permittivity (corresponding to the blue box and purple circle, respectively) using the $TE_{01\delta}$ method are quite close to that of the both extrapolated values from fitting data of far infrared. Therefore, it can be concluded that in the microwave region, the polarization of Li_3MgNbO_5

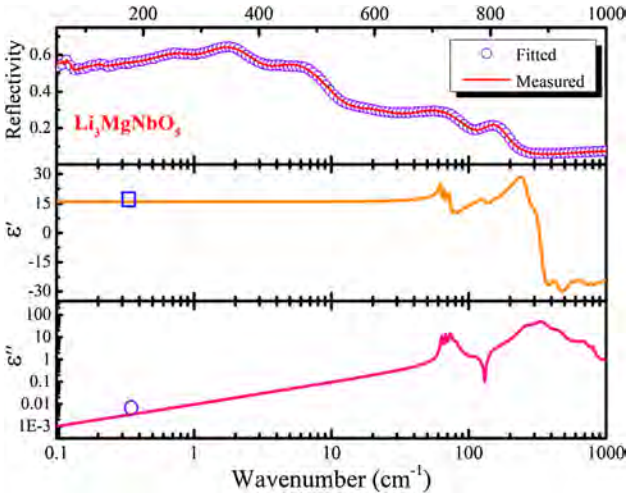

Figure 5 Measured and fitted infrared reflectivity spectra and the real and imaginary parts of complex dielectric response of Li_3MgNbO_5 ceramics.

ceramic was mainly caused by photon absorption in the infrared region.

From the perspective of the application, a near-zero TCF value is indispensable, which can eliminate the temperature drift of the resonant frequency characteristic of the dielectrics. In the current work, the traditional positive TCF compensator of $CaTiO_3$ was selected to counteract the negative TCF value of Li_3MgNbO_5 ceramic. Figure 6 shows the X-ray diffraction patterns, BSE image, and EDS analysis results of $0.96Li_3MgNbO_5$–$0.04CaTiO_3$ ceramics sintered at 1260 °C. The independent diffraction peaks of Li_3MgNbO_5 and $CaTiO_3$ and grains with different grays (the marked darker grains belonged to $CaTiO_3$) could be found in XRD and BSE results, suggesting no chemical reaction between them. Table 4 lists the

Table 3 Phonon parameters obtained by fitting of the infrared reflectivity spectra of Li_3MgNbO_5 ceramic

Mode	ω_{oj}	ω_{pj}	γ_j	$\Delta\varepsilon_j$
1	129.89	89.86	16.16	4.68
2	179.64	84.66	32.93	2.27
3	266.30	653.57	72.85	1.02
4	337.42	1171.30	93.95	2.00
5	446.86	853.51	117.44	0.65
6	598.45	542.19	145.91	0.82
7	697.94	625.79	131.29	0.80
8	800.86	260.20	48.68	0.11
Li_3MgNbO_5	ε_∞ = 3.55		ε_0 = 15.9	

microwave dielectric properties of composite $(1-x)Li_3MgNbO_5$–$xCaTiO_3$ ceramics. A near-zero TCF value of + 1.2 ppm/°C associated with an ε_r of 18.4 and $Q \times f$ value of 86625 GHz was achieved for composite $0.96Li_3MgNbO_5$–$0.04CaTiO_3$ ceramics sintered at 1260 °C.

Plot of $Q \times f$ versus ε_r of Li_3MgNbO_5 ceramic and recently reported representative solid solutions ceramics with cubic rock-salt structured is displayed in Fig. 7 [11–24, 38–44]. The characteristics of these ceramics are low ε_r and high $Q \times f$ value. Among them, except for the Li_2AO_3–BO (A = Mg, Zn, Ni; B = Ti, Sn, Zr) system mentioned in the part of introduction, it is worth noting that some low-firing oxyfluoride microwave dielectric materials such as $Li_5Ti_2O_6F$, $Li_7Ti_3O_9F$, and $Li_{3.1}W_{0.7}F_{0.3}O_{3.5}$ have recently studied in Li_2TiO_3–LiF, and Li_4WO_5–LiF systems, which exhibited great potential for LTCC applications [42–44].

Conclusions

In this work, a novel rock-salt type Li_3MgNbO_5 ceramic was fabricated through the solid-state sintering route. Rietveld refinements, SEAD pattern, and HRTEM confirmed that Li_3MgNbO_5 crystallized in the cubic rock-salt structure with Fm-3 m space group. The evolution of microstructures was consistent with the change trend of relative density and MDPs. Optimum MDPs with ε_r of 16.2, $Q \times f$ of 96796 GHz, and TCF value of − 24.8 ppm/°C were obtained at 1260 °C/4 h for Li_3MgNbO_5 ceramic. The fitting results of the infrared reflectivity spectra were very close to the measured ones. Lastly, the temperature stability of ceramics was counteracted by $CaTiO_3$ and the resultant $0.96Li_3MgNbO_5$–$0.04CaTiO_3$ possessed a satisfactory comprehensive dielectric performance (ε_r = 18.4, $Q \times f$ = 86625 GHz, and TCF = + 1.2 ppm/°C).

Acknowledgements

This work was supported by Natural Science Foundation of China (Nos. 21761008 and 21965009), the Natural Science Foundation of Guangxi Zhuang Autonomous Region (Nos. 2018GXNSFAA138175, 2018GXNSFBA281093), and Projects of Department of Science and Technology of Guangxi (Nos.

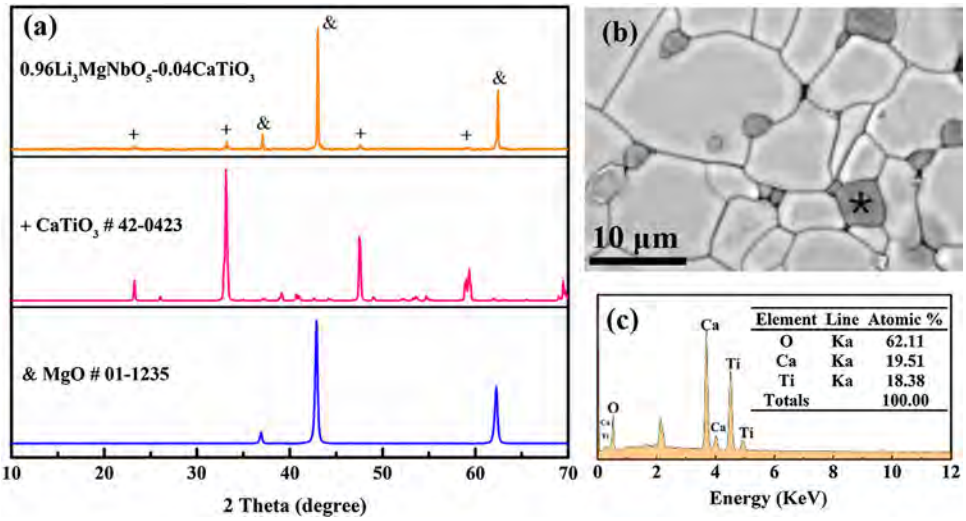

Figure 6 **a** X-ray diffraction patterns, **b** BSE image, and **c** EDS analysis results of $0.96Li_3MgNbO_5$-$0.04CaTiO_3$ ceramics sintered at 1260 °C.

Table 4 Microwave dielectric properties of composite $(1-x)Li_3MgNbO_5$–$xCaTiO_3$ ceramics

x value	S.T. (°C)	ε_r	$Q \times f$ (GHz)	TCF (ppm/°C)
0	1260	16.2	96796	− 24.8
0.02	1260	17.6	92470	− 13.5
0.03	1260	18.0	89914	− 5.7
0.04	1260	18.4	86625	+ 1.2
0.05	1260	18.9	79540	+ 8.4

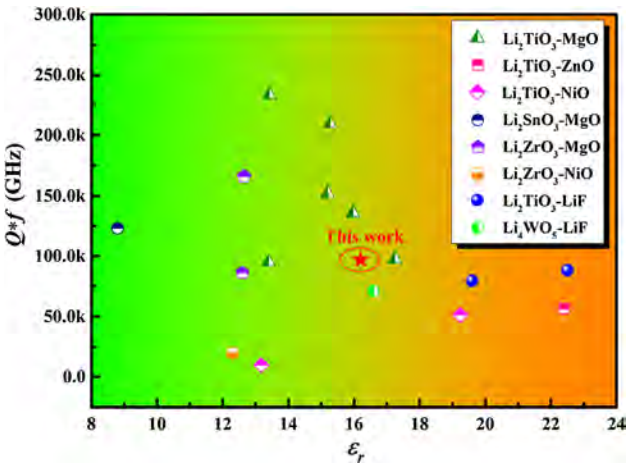

Figure 7 Comparison of $Q \times f$ values as a function of ε_r for cubic rock-salt structure ceramics.

AA18118008, AA18118034, and AA18118023), Projects of Department of Education of Guangxi (No. 2018Ky0255), High Level Innovation Team and Outstanding Scholar Program of Guangxi Institutes and Innovation Project of Guangxi Graduate Education (YCBZ2020167 and YCBZ2020066).

References

[1] Cava RJ (2001) Dielectric materials for applications in microwave communications. J Mater Chem 11:54–62

[2] Ohsato H (2012) Functional advances of microwave dielectric for next generation. Ceram Int 38:S141–S146

[3] Vanderah TA (2002) Talking ceramics. Science 298:1182–1184

[4] Sebastian MT, Ubic R, Jantunen H (2015) Low-loss dielectric ceramic materials and their properties. Int Mater Rev 60:392–412

[5] Sebastian MT, Jantunen H (2008) Low loss dielectric materials for LTCC applications: a review. Int Mater Rev 53:57–90

[6] Alford NM, Penn SJ (1996) Sintered alumina with low dielectric loss. J Appl Phys 80:5895–5898

[7] Sugiyama T, Tsunooka T, Kakimoto K, Ohsato H (2006) Microwave dielectric properties of forsterite based solid solutions. J Eur Ceram Soc 26:2097–2100

[8] Matsumoto H, Tamura H, Wakino K (1991) $Ba(Mg, Ta)O_3$–$BaSnO_3$ high Q dielectric resonator. Jpn J Appl Phys 30:2347–2349

[9] Barber DJ, Moulding KM, Zhou J, Li MQ (1997) Structural order in $Ba(Zn_{1/3}Ta_{2/3})O_3$, $Ba(Zn_{1/3}Nb_{2/3})O_3$ and $Ba(Mg_{1/3}Ta_{2/3})O_3$ microwave dielectric ceramics. J Mater Sci 32:1531–1544. https://doi.org/10.1023/A:1018574505601

[10] Zhou HF, Tan XH, Chen XL (2018) Effect of raw materials pretreated by physical grinding method on the sintering ability and microwave dielectric properties of Li_2MgTiO_4 ceramics. J Alloy Compd 731:839–843

[11] Tseng YW, Chen JY, Kuo YC, Huang CL (2011) Low-loss microwave dielectrics using rock salt oxide Li_2MgTiO_4. J Alloy Compd 509:L308–L310

[12] Bi JX, Niu YJ, Wu HT (2017) $Li_4Mg_3Ti_2O_9$: a novel low-loss microwave dielectric ceramic for LTCC applications. Ceram Int 43:7522–7530

[13] Li CC, Xiang HC, Yin CZ, Tang Y, Li YC, Fang L (2018) Ultra-low loss microwave dielectric ceramic $Li_2Mg_2TiO_5$ and low-temperature firing via B_2O_3 addition. J Electron Mater 47:6383–6389

[14] Pan HL, Wu HT (2017) Crystal structure, infrared spectra and microwave dielectric properties of new ultra low-loss $Li_6Mg_7Ti_3O_{16}$ ceramics. Ceram Int 43:14484–14487

[15] Fu ZF, Liu P, Ma JL, Chen XM, Zhang HW (2016) New high Q low-fired $Li_2Mg_3TiO_6$ microwave dielectric ceramics with rock salt structure. Mater Lett 164:436–439

[16] Bi JX, Li CC, Zhang YH, Xing CF, Yang CH, Wu HT (2017) Crystal structure, infrared spectra and microwave dielectric properties of ultra low-loss $Li_2Mg_4TiO_7$ ceramics. Mater Lett 196:128–131

[17] Zhang X, Tang B, Fang ZX, Yang HY, Xiong Z, Xue LX, Zhang SR (2018) Structural evolution and microwave dielectric properties of a novel $Li_3Mg_{2-x/3}Nb_{1-2x/3}Ti_xO_6$ system with a rock salt structure. Inorg Chem Front 5:3113–3125

[18] Zhang X, Jiang ZH, Tang B, Fang ZX, Xiong Z, Li H, Yuan CL, Zhang SR (2020) A new series of low-loss multicomponent oxide microwave dielectrics with a rock salt structure: Li_5MgABO_8 (A = Ti, Sn; B = Nb, Ta). Ceram Int 46:10332–10340

[19] Castellanos M, West AR (1979) Order-disorder phenomena in oxides with rock salt structures: the system Li_2TiO_3–MgO. J Mater Sci 14:450–454. https://doi.org/10.1007/BF00589838

[20] Bian JJ, Dong YF (2010) New high Q microwave dielectric ceramics with rock salt structures: $(1–x)Li_2TiO_3+xMgO$ system ($0 \le x \le 0.5$). J Eur Ceram Soc 30:325–330

[21] Fu ZF, Liu P, Ma JL, Zhao XG, Zhang HW (2016) Novel series of ultra-low loss microwave dielectric ceramics: $Li_2Mg_3BO_6$ (B=Ti, Sn, Zr). J Eur Ceram Soc 36:625–629

[22] Zuo RZ, Zhang J, Song J, Xu YD (2017) Liquid-phase sintering, microstructural evolution, and microwave dielectric properties of $Li_2Mg_3SnO_6$–LiF ceramics. J Am Ceram Soc 101:569–576

[23] Bi JX, Xing CF, Yang CF, Wu HT (2018) Phase composition, microstructure and microwave dielectric properties of rock salt structured Li_2ZrO_3–MgO ceramics. J Eur Ceram Soc 38:3840–3846

[24] Xing CF, Liu FL, Bi JX, Wu HT (2018) Low-temperature sintering and microwave dielectric properties of LiF doped $0.2Li_2ZrO_3$–0.8MgO ceramics. J Mater Sci Mater Electron 29:13746–13750

[25] Yuan LL, Bian JJ (2009) Microwave dielectric properties of the lithium containing compounds with rock salt structure. Ferroelectrics 387:123–129

[26] Bian JJ, Liang Z, Wang L (2011) Structural evolution and microwave dielectric properties of $Li_{(3-3x)}M_{4x}Nb_{(1-x)}O_4$ (M=Mg, Zn; $0 \le x \le 0.9$). J Am Ceram Soc 94:1447–1453

[27] Zhang ZW, Tang Y, Li J, Chen JQ, Yang AH, Wang Y, Zhai YF, Ao LY, Su CX, Xing XR, Fang L (2020) High-Q and near-zero τ_f composite $Li_2Mg_2TiO_5$-$Sr_3(VO_4)_2$ ceramics for low-temperature co-fired ceramic applications. Ceram Int 46:8281–8286

[28] Leach C, Vernonparry KD (2006) The effect of sintering temperature on the development of grain boundary traps in zinc oxide based varistors. J Mater Sci 41:3815–3819. https://doi.org/10.1007/s10853-006-7066-x

[29] Chen I (2000) Grain boundary kinetics in oxide ceramics with the cubic fluorite crystal structure and its derivatives. Interf Sci 8:147–156

[30] Xiong Z, Tang B, Luo FC, Yang HY, Zhang X, Yang CT, Fang ZX, Zhang SR (2020) Characterization of structure, chemical bond and microwave dielectric properties in $Ca_{0.61}Nd_{0.26}TiO_3$ ceramic substituted by chromium for titanium. J Alloy Compd 835:155249

[31] Martirena HT, Burfoot JC (1974) Grain-size effects on properties of some ferroelectric ceramics. J Phys C Solid State Phys 7:3182–3192

[32] Bosman AJ, Havinga EE (1963) Temperature dependence of dielectric constants of cubic ionic compounds. Phys Rev 129:1593–1600

[33] Shannon RD (1993) Dielectric polarizabilities of ions in oxides and fluorides. J Appl Phys 73:348–366

[34] Yoon SH, Kim DW, Cho SY, Hong KS (2006) Investigation of the relations between structure and microwave dielectric properties of divalent metal tungstate compounds. J Eur Ceram Soc 26:2051–2054

[35] Sebastian MT (2008) Dielectric materials for wireless communication. Elsevier, Amsterdam

[36] Lin IN, Chia CT, Liu HL (2007) Intrinsic dielectric and spectroscopic behavior of perovskite $Ba(Ni_{1/3}Nb_{2/3})O_3$–$Ba(Zn_{1/3}Nb_{2/3})O_3$ microwave dielectric ceramics. J Appl Phys 102:044112

[37] Guo J, Zhou D, Wang L, Wang H, Shao T, Qi ZM, Yao X (2013) Infrared spectra, Raman spectra, microwave dielectric properties and simulation for effective permittivity of temperature stable ceramics $AMoO_4$–TiO_2 (A = Ca, Sr). Dalton Trans 42:1483–1491

[38] Huang CL, Tseng YW, Chen JY (2012) High-Q dielectrics using ZnO-modified Li_2TiO_3 ceramics for microwave applications. J Eur Ceram Soc 32:3287–3295

[39] Lyu XS, Li LX, Cai HC, Sun H (2015) A new microwave dielectric material $LiNi_{0.5}Ti_{0.5}O_2$. Ceram Int 41:9168–9171

[40] Liu QQ, Pan HL, Tao WH, Wu HT (2017) New rock salt structure dielectric material $Li_2Ni_3TiO_6$ at microwave frequency. J Mater Sci Mater Electron 28:9893–9899

[41] Jiang PB, Hu YD, Bao SX, Chen J, Duan ZZ, Hong T, Wu CH, Wang G (2019) A novel microwave dielectric ceramic Li_2NiZrO_4 with rock salt structure. RSC Adv 9:32936–32939

[42] Zhang ZW, Tang Y, Xiang HC, Yang AH, Wang Y, Yin CZ, Tian YF, Fang L (2020) $Li_5Ti_2O_6F$: a new low-loss oxyfluoride microwave dielectric ceramics for LTCC applications. J Mater Sci 55:107–115. https://doi.org/10.1007/s10853-019-04031-4

[43] Zhang ZW, Fang L, Xiang HC, Xu MY, Tang Y, Jantunen H, Li CC (2019) Structural, infrared reflectivity spectra and microwave dielectric properties of the $Li_7Ti_3O_9F$ ceramic. Ceram Int 45:10163–10169

[44] Xiao K, Li C, Tang Y, Tian Y, Yin C, Chen J, Fang L (2020) $(1–x)Li_4WO5$-xLiF: a novel oxyfluoride system and their microwave dielectric properties. J Alloys Compd 835:155320. https://doi.org/10.1016/j.jallcom.2020.155320